

ARTICLE OPEN



The impacts of the atmospheric boundary layer on regional haze in North China

Qianhui Li¹, Hongsheng Zhang¹✉, Xuhui Cai², Yu Song² and Tong Zhu²

An intensive atmospheric boundary layer (ABL) experiment was conducted simultaneously at six stations arranged in a cross shape on the North China Plain (NCP) from 26 November to 26 December 2019. The impacts of the regional ABL structure on heavy haze pollution and the relationship between the ABL height and aerosol accumulation layer (AAL) depth were discussed. Bouts of downdrafts generate a persistent descending elevated inversion layer, helping the maintenance and exacerbation of haze pollution. Continuous weak wind layers contribute to the pollutants accumulation, and low-level jets promote the removal of air pollutants. The unique landform conditions of the NCP are reflected in its regional ABL structure and further affect the spatial distribution of haze pollution. Due to the drainage flow and strong downdrafts, the western stations near the mountains have a colder surface and warmer upper air masses, resulting in a more stable stratification and worse diffusion conditions; these stations also experience a thicker weak wind layer caused by increased friction. Thus, the spatial distribution of haze is heavier in the west and lighter in the east. The convective boundary layer (CBL) height declines evidently during haze episodes, usually lower than 560 m. Furthermore, as the vertical distribution of aerosols is mainly influenced by daytime thermal turbulence and maintained at night, it is appropriate to determine the CBL height using the AAL depth. However, the AAL depth is not consistent with the stable boundary layer height due to the influence of the residual layer at night.

npj Climate and Atmospheric Science (2021)4:9; <https://doi.org/10.1038/s41612-021-00165-y>

INTRODUCTION

Frequent haze pollution events represent one of the most serious atmospheric environmental problems faced by China, as they result in poor air quality and low visibility^{1–3}. Fine particulate matter, known as PM_{2.5} (particulate matter with an aerodynamic diameter no greater than 2.5 μm), is the chief pollutant^{4,5}. Haze pollution shows considerable seasonal variations and regional disparities. Seasonally, it is generally more serious in winter^{6,7}. Spatially, the North China Plain (NCP), the Yangtze River Delta (YRD), the Pearl River Delta (PRD), and the Sichuan Basin (SB) have been recognized as four major haze regions in China^{8–11}. The NCP has become the most polluted district in China¹². And the effects of its unique topography and local circulation on haze pollution in the NCP have attracted wide attention of researchers^{13–19}.

The formation mechanisms of long-lasting winter haze pollution events characterized by high PM_{2.5} concentrations have been investigated from various perspectives and on different scales^{20–24}. In general, persistent heavy haze events are associated with a high emission background^{25,26}, adverse meteorological conditions^{27–30}, regional transport^{31–33}, and secondary aerosol formation^{34–36}. In particular, the meteorological conditions in the atmospheric boundary layer (ABL), which determines the vertical transport of heat, water vapor and aerosols between the underlying surface and atmosphere, are crucial to haze dispersion³⁷. Strong inversions and stagnant winds are favorable conditions for the accumulation of pollutants, and high humidity can contribute to the hygroscopic growth and secondary formation of aerosols^{38,39}. The diurnal variation of the ABL can result in variations in the PM_{2.5} concentration^{40,41}. In the daytime ABL, known as the convective boundary layer (CBL), PM_{2.5} can be mixed uniformly in a thick layer due to the active turbulent mixing⁴². While in the nighttime ABL, also called the stable boundary layer (SBL), high PM_{2.5} concentrations are often observed near the surface due to the stable stratification and

intermittent turbulence^{43–45}. Moreover, pollutants in the residual layer can be mixed downward to the surface with the development of the ABL the next morning^{16,46,47}. Regarding the dynamic structure, low-level jets (LLJs) and turbulent motions can modify the air quality by affecting transport and diffusion capabilities. LLJs can not only contribute to the advection of pollutants to less polluted areas⁴⁸, but also improve air quality in the pollution dissipation stage by triggering turbulent mixing and transferring momentum downward^{49,50}.

The atmospheric boundary layer height (ABLH) is an important parameter in air quality assessments that reflects the effects of turbulent mixing, convection and other physical processes in the ABL⁵¹. Studies have shown that the ABLH is a main meteorological driver of PM_{2.5} variation⁵². There is a negative correlation between the ABLH and pollutant concentrations^{53–55}. The ABLH in winter is lower than that in summer, which makes haze pollution form more easily in winter^{56,57}. In addition, with the rapid development of ground-based remote sensing equipment, such as lidars and ceilometers, a number of studies have attempted to retrieve the ABLH based on the distributions of substances^{58–60}. The theoretical basis of this approach is that aerosols are abundant in the ABL, but sharply decrease at the boundary layer top, while the free atmosphere is free of aerosols⁶¹.

With the increasing attention paid to the impacts of the ABL on haze pollution, many field experiments have been conducted. Atmospheric profiles have commonly been acquired by meteorological towers, tethered balloons, conventional radiosondes and surface-based remote sensing equipment^{47,62–65}. However, boundary layer observations are still scarce overall, the influence of the ABL structure on heavy haze pollution remains to be studied. And most studies were based on single-station observations, whereas joint observations of the spatial distribution of haze pollution and the regional ABL structure are lacking. In addition,

¹Laboratory for Climate and Ocean-Atmosphere Studies, Department of Atmospheric and Oceanic Sciences, School of Physics, Peking University, Beijing, China. ²State Key Joint Laboratory of Environmental Simulation and Pollution Control, College of Environmental Sciences and Engineering, Peking University, Beijing, China. ✉email: hsdq@pku.edu.cn

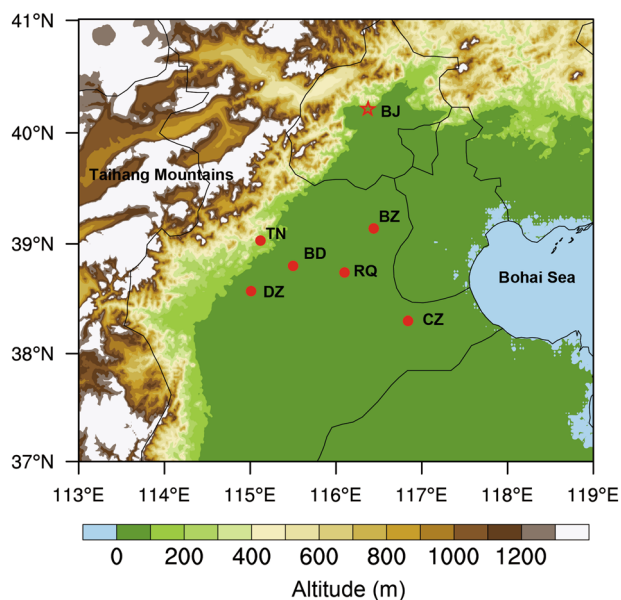


Fig. 1 Geographical locations of the six observation stations. TN, BD, RQ, CZ, BZ, and DZ represent Tuonan, Baoding, Renqiu, Cangzhou, Bazhou, and Dingzhou stations, respectively. The red star is the location of the capital city, Beijing (BJ).

the relationship between the aerosol accumulation layer (AAL) depth (see Section “Determination of the ABLH and AAL depth” for the definition) and ABLH needs to be further clarified. To investigate these topics, an intensive ABL field experiment was carried out at six stations in the NCP for a month during the winter of 2019. The six observation stations were arranged in the shape of a cross (Fig. 1), and regional profiles of atmospheric meteorological elements and $PM_{2.5}$ concentrations were collected by high-resolution GPS sounding. Details of the field experiment and data can be found in Section “Observation stations and instruments” and Section “Data acquisition and processing”. Based on the observational data, the following three questions were studied: First, the characteristics of the ABL structure during persistent heavy haze pollution. Second, regional ABL structure and its impacts on spatial distribution of haze pollution. Third, the relationship between the ABLH and AAL depth.

RESULTS

Overview of fog-haze pollution during the observation period

According to the National Environmental Protection Standards of China HJ 633-2012, the ambient air quality can be divided into six grades, namely excellent (level 1, AQI is between 0 and 50), good (level 2, AQI is between 51 and 100), light pollution (level 3, AQI is between 101 and 150), moderate pollution (level 4, AQI is between 151 and 200), heavy pollution (level 5, AQI is between 201 and 300), and severe pollution (level 6, AQI is larger than 300), respectively. During the observation period, three serious air pollution events with $PM_{2.5}$ as the primary pollutant reached moderate or heavy pollution levels. As shown in Fig. 2, Case 1 ranges from 20:00 local time (LT) on 28 November to 20:00 LT on 1 December 2019, Case 2 is from 20:00 LT on 6 December to 8:00 LT on 11 December 2019, and Case 3 is from 14:00 LT 21 December to 8:00 LT 26 December 2019. The temporal variations of the surface meteorological elements observed at Renqiu station are also shown in Fig. 2. During these haze episodes, the diurnal variation of temperature (T) is weak. The specific humidity (q) is relatively higher in the pollution period but drops rapidly in the cleaning period. In hazy weather, the wind speed (WS) is mostly smaller than 2 m s^{-1} , which is favorable for the formation of haze

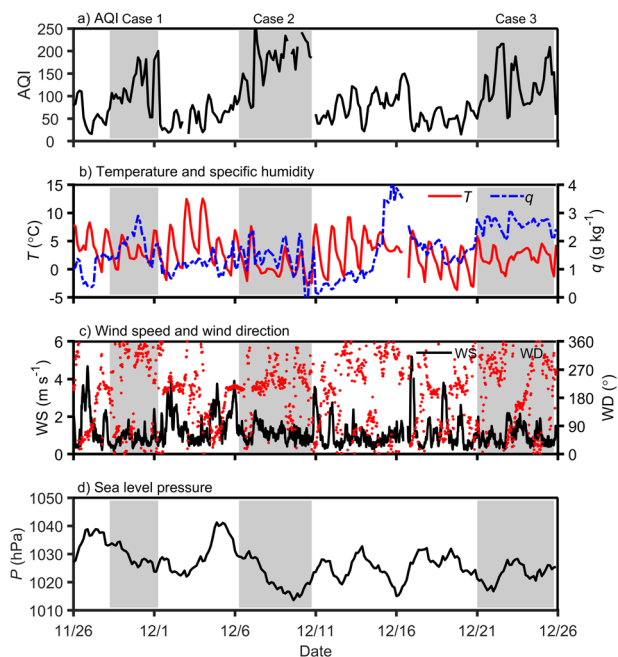


Fig. 2 Temporal variations of air quality and meteorological factors in the surface layer at Renqiu station during the observation period. **a** air quality index (AQI), **b** temperature (T) and specific humidity (q), **c** wind speed (WS), and wind direction (WD), **d** sea level pressure (P). The shaded areas represent three haze episodes.

pollution; while it increased obviously to $\sim 4\text{ m s}^{-1}$ during the cleaning period. The weather condition is relatively stable during the pollution period. As Fig. 2d depicts, the surface pressure (P) field changes slowly and has successive low pressures during heavy and long-lasting haze pollution, and this pressure pattern is consistent with the previous study⁶⁶.

Figure 3 illustrates a comparison of the pollution level and surface meteorological elements among Tuonan, Baoding, and Renqiu stations during the whole observation period. Figure 3a shows that Tuonan has the best air quality with excellent or good air quality accounting for $\sim 70\%$, while the air quality is the worst in Baoding with only 30% observations under clean weather and most frequent heavy pollution events. In brief, Baoding experiences the worst haze pollution, Renqiu follows, and Tuonan has the best air quality. There are significant differences in the surface meteorological elements among the different stations. Wind speeds smaller than 1 m s^{-1} account for 71%, 66%, and 55% of all wind speeds during the observation period at the Tuonan, Baoding, and Renqiu stations, respectively; these percentages suggest that the wind tends to be calmer in Tuonan but stronger in Renqiu. The proportions of temperatures less than 0°C are 71%, 46%, and 18% in Tuonan, Baoding, and Renqiu, respectively, indicating that Tuonan has the coldest surface, while Renqiu has the warmest. In addition, the daily temperature range in Tuonan is the largest among the three stations while that in Renqiu is the smallest. The specific humidity is relatively high at Baoding station, while it tends to be drier at Tuonan and Renqiu stations. Based on the above comparison, the wind speed increases from the western mountain area to the eastern plain, and the temperature has a similar trend. These features can be attributed to the influence of the mountains in western NCP. Due to increased friction near the mountains, the wind speeds are significantly weakened^{6,37}. In addition, cold air masses slide down the mountains at night, forming cold air pools in the valley⁶⁷. Because there is less water vapor transport from the southerly wind in Baoding than Renqiu and Tuonan, and Baoding has a denser population and advanced

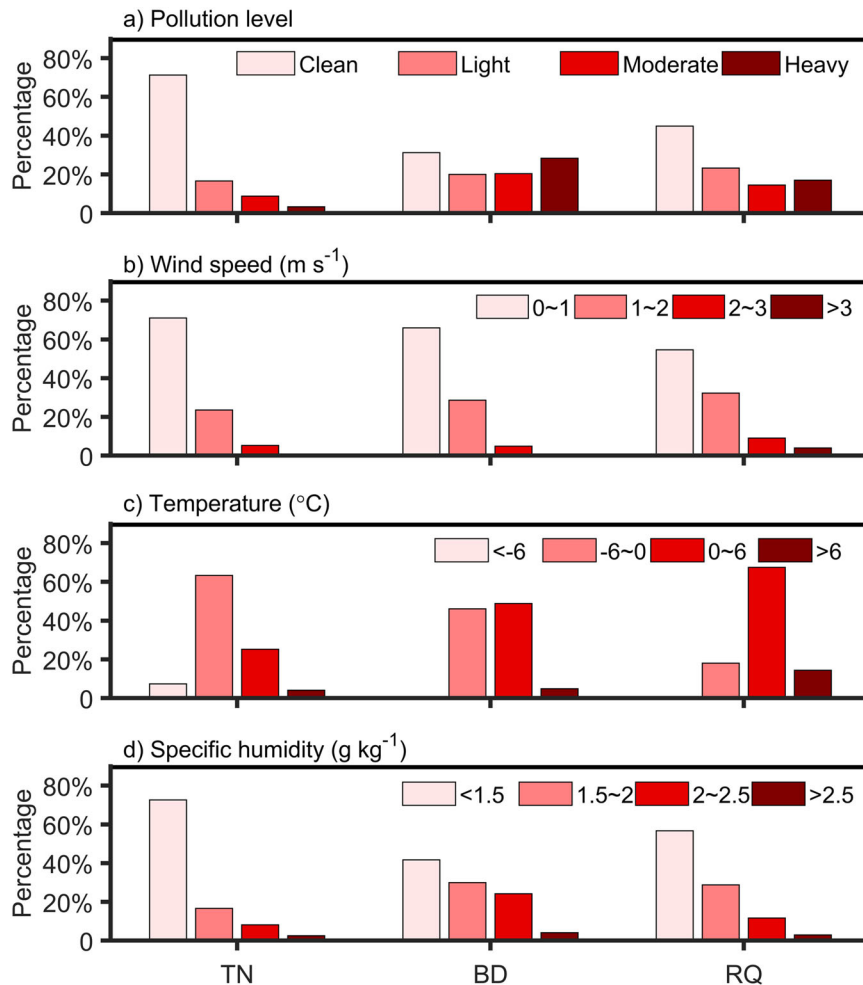


Fig. 3 Comparison of the pollution level and surface meteorological elements among Tuonan (TN), Baoding (BD), and Renqiu (RQ) stations during the whole observation period. (a) pollution level (clean represents the air quality is excellent or good; light, moderate and heavy represent three levels of pollution), (b) wind speed, (c) temperature, (d) specific humidity.

industry than the other two areas^{27,68}, thus the higher moisture at the Baoding station is more likely to be related to local anthropogenic emissions.

Impacts of the ABL structure on persistent heavy haze pollution

Among all three haze pollution cases captured during the observation period, Case 2 arouses the greatest concern, as this persistent event was the most polluted. From 6 to 11 December 2019, this event lasted for more than 4 days, and the $PM_{2.5}$ concentration in the surface layer even exceeded $200 \mu\text{g m}^{-3}$. As the pollution process and ABL structure are similar at six stations, the pattern of Baoding station is given here only. Figure 4a depicts the temporal variation of the vertical $PM_{2.5}$ concentration distribution, or in other words, the temporal variation of the AAL. As the strong southwest wind appeared and promoted the advection transport of pollutants on 6 December, the early AAL characterized by large thickness (~ 1000 m) but light pollution ($PM_{2.5}$ concentration smaller than $100 \mu\text{g m}^{-3}$) was formed. Then, in the accumulation stage of pollution, $PM_{2.5}$ was mainly concentrated in a shallow layer below 800 m. And after 8 December, the AAL depth showed a continuous declining trend and dropped to ~ 200 m on 11 December, and the haze pollution became further aggravated. Finally, the pollution was rapidly removed by the northerly jet stream and the AAL disappeared on 11 December.

Figure 4b shows that the variation of the AAL is closely related to the thermal ABL structure. From 8 to 11 December, there was a thick elevated inversion layer at relatively low altitudes all the time, and the bottom of the elevated inversion layer decreased gradually, corresponding to the decrease in the AAL depth. It is clear that fine particles were confined below the strong elevated inversion layer, and their vertical distribution changed with the regulation of the thermal structure. This is because the inversion layer exhibits stable stratification, which restricts vertical turbulent transport to a great extent. Therefore, it is difficult for pollutants to pass through the inversion layer. The persistent existence of inversions results in long-lasting adverse vertical diffusion conditions, which is conducive to the accumulation of aerosols and water vapor. A decrease in the bottom height of the inversion layer further worsens the diffusion conditions, concentrating aerosols and water vapor in a shallower layer. The descending elevated inversion layer may be attributed to bouts of sinking motions. In this haze event, a trough was stable at low altitudes over the North China Plain and deepened with the intrusion of gusty cold air along its western flank, which caused constant sinking motions. Figure 5 shows the vertical velocity (ω) at 8:00 LT on 8–10 December 2019, the positive values of ω represent sinking motions. It is clear that the downdrafts were gradually intensified from 8 to 10 December 2019, especially over the western stations near Taihang Mountains. Such downdrafts can cause the upper air to warm up, resulting in the formation of an elevated inversion layer. In summary, persistent descending inversion layers

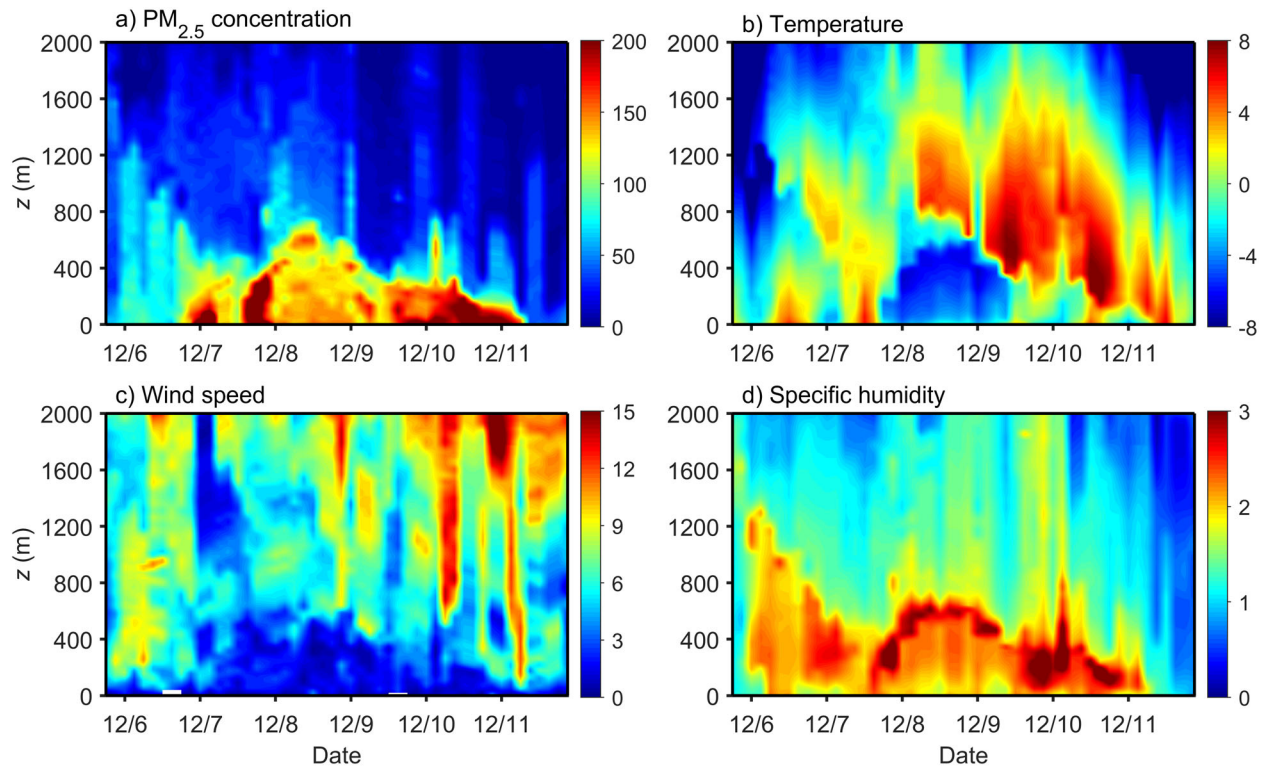


Fig. 4 Temporal variations of the vertical distributions of air pollutants and atmospheric boundary layer structure at Baoding station from 6 to 11 December 2019. **a** $\text{PM}_{2.5}$ concentration (unit: $\mu\text{g m}^{-3}$), **(b)** temperature (unit: $^{\circ}\text{C}$), **(c)** wind speed (unit: ms^{-1}), and **(d)** specific humidity (unit: g kg^{-1}).

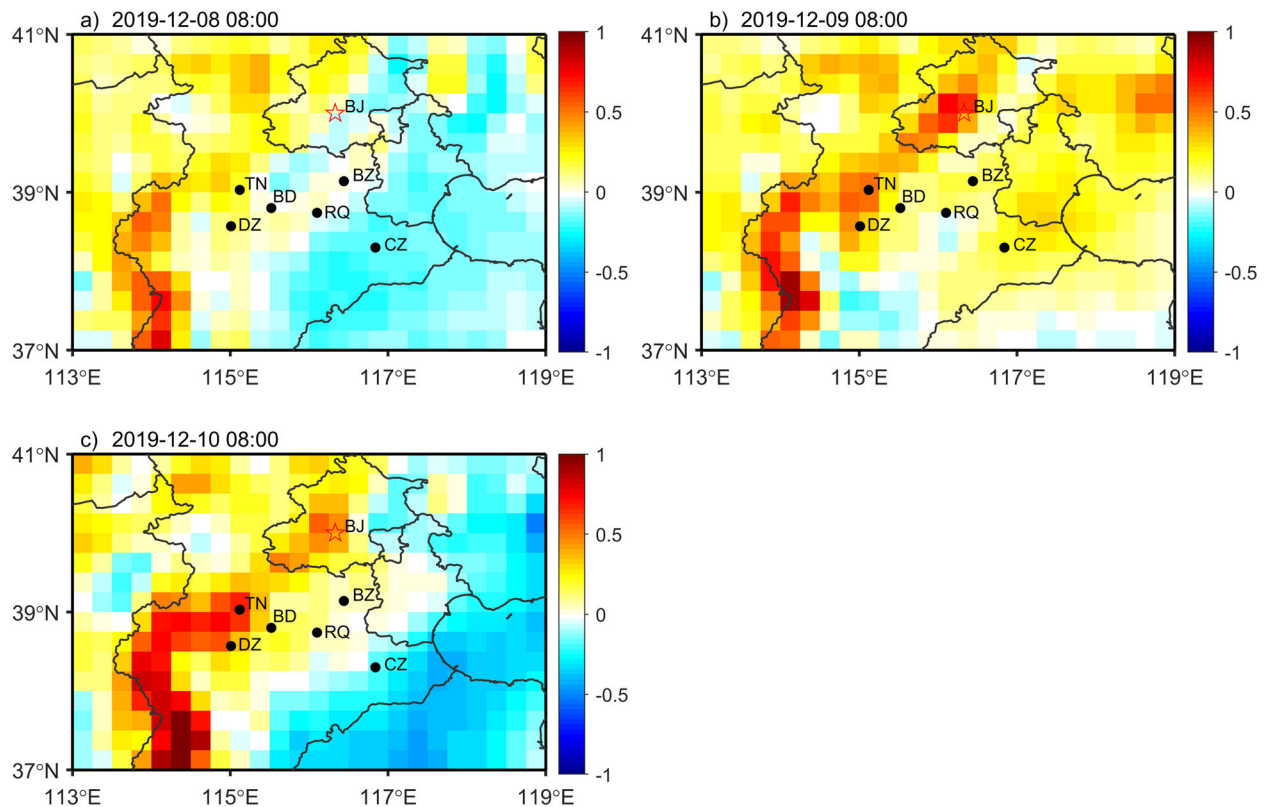


Fig. 5 Vertical velocity at 925 hPa at 8:00 LT from 8 to 10 December 2019. **a–c** shows the vertical velocity (unit: Pa s^{-1}) on 8, 9, and 10 December, respectively.

play a key role in the maintenance and exacerbation of heavy haze pollution.

As shown in Fig. 4c, the AAL is also closely related to the dynamic structure of the ABL. In the transport stage, there is strong southwest wind throughout the ABL, making the $PM_{2.5}$ concentration gradually increase in the whole layer, and the AAL depth can reach 1000 m. In the accumulation stage, weak or calm winds (usually smaller than 2 ms^{-1}) are dominant in the AAL. This dynamic condition, which implies the poor horizontal transport capacity of pollutants, also greatly contributes to the accumulation of $PM_{2.5}$ in local areas. The small wind layer, like the AAL, lies below the elevated inversion layer, and its formation is associated with the inversion layer. Due to the existence of the thick and strong elevated inversion layer, the turbulent transport is greatly inhibited. And the weak turbulent transport makes it difficult for the larger momentum in upper layer to be transported downward. As a consequence, the wind speed remains at low values beneath the elevated inversion layer, forming a small wind layer. Finally, haze pollution is cleared by a strong wind jet stream reaching the ground, which not only increases the horizontal transport capacity but also improves the vertical diffusion conditions by promoting the generation of mechanical turbulence. Therefore, heavy haze pollution is accompanied by weak winds, and the low-level jet is a key factor in the removal of air pollutants.

Figure 4d depicts the humidity structure of the ABL, which also has an impact on haze pollution. Heavily polluted areas are consistent with areas characterized by high humidity. In the early stage of haze pollution, this configuration reflects the regional transport of pollutants and water vapor from southwestern areas. During the maintenance stage of haze pollution, the consistency indicates the synchronous accumulation of pollutants and water vapor in the lower atmosphere under poor diffusion conditions. The mitigation of haze pollution from 8 to 9 December might be attributed to the fog. In foggy weather, some aerosols can act as condensation nuclei and be converted into fog droplets, and some aerosols can be removed through wet scavenging^{62,69}.

Spatial distribution of haze pollution and regional ABL structure

Surrounded by mountains to the north and west and bounded by the sea to the east, the special geographical position of the NCP leads to significant differences in both the ABL structure and the spatial distribution of haze pollution over this region^{12,15,70}. We have noticed that regional pollution pattern often reflects higher pollution levels in the western part of the NCP during the observation period. Figure 6a shows the regional spatial distribution of the $PM_{2.5}$ concentration at 14:00 LT on 30 November 2019. In terms of the pollution level, haze pollution was the heaviest at the Baoding and Dingzhou stations, with $PM_{2.5}$ concentrations exceeding $200 \mu\text{g m}^{-3}$ in the pollution center with a depth of ~ 700 m. The Renqiu and Bazhou stations experienced the lightest haze pollution with the thinnest AAL, where the $PM_{2.5}$ concentration was less than $100 \mu\text{g m}^{-3}$ and the AAL was lower than 500 m. In addition, the pollution level was moderate at the Tuonan and Cangzhou stations, where the AAL was thick (~ 1000 m) in Cangzhou and thin (~ 500 m) in Tuonan.

The corresponding regional thermal structure of the ABL is shown in Fig. 6b. The surface temperature increases from the west (Tuonan) to the east (Cangzhou). Closer to the mountains, the stations in the west are more influenced by nighttime drainage flow, resulting in the accumulation of cold air masses in the surface layer. As depicted in Fig. 6b, there is a strong and thick elevated inversion layer over the stations to the west (Tuonan, Baoding, and Dingzhou), while the stations in the east (Renqiu, Bazhou, and Cangzhou) do not exhibit this feature. This indicates that the warming effect induced by the downdrafts is stronger in areas near the mountains. As a consequence, stations located to the west have a colder surface and warmer upper air masses,

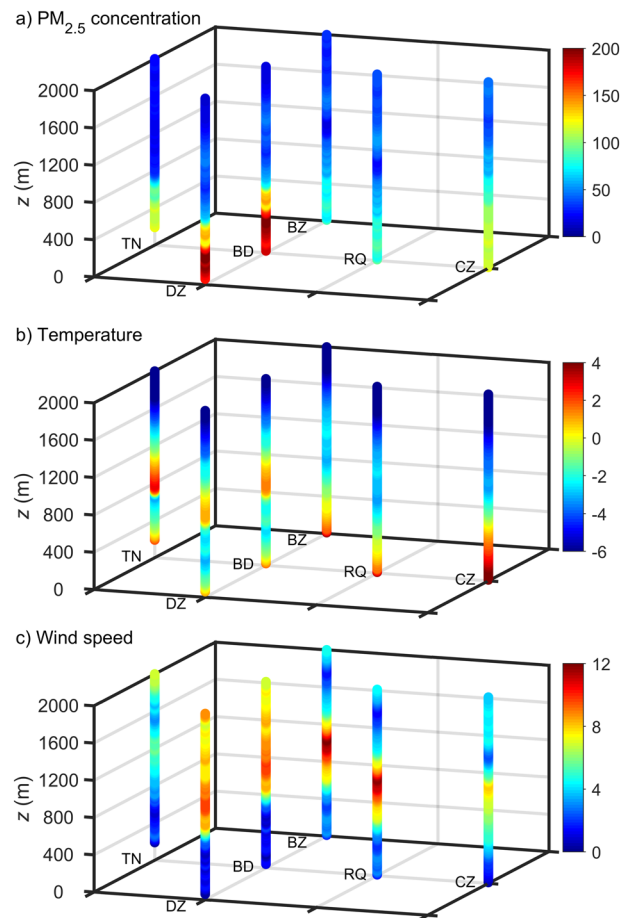


Fig. 6 Spatial distributions of air pollutants and the corresponding regional ABL structure at 14:00 LT on 30 November 2019. **a** $PM_{2.5}$ concentration (unit: $\mu\text{g m}^{-3}$), **(b)** temperature (unit: $^{\circ}\text{C}$), **(c)** wind speed (unit: ms^{-1}).

which means a more stable stratification that can greatly suppress the vertical transport of air pollutants. This is one of the reasons why the western sites are more polluted than the eastern sites.

As for the dynamic structure of the ABL, Fig. 6c shows that the western sites (Tuonan, Baoding, and Dingzhou) possess a thicker layer (~ 500 m) with much calmer wind speeds (smaller than 2 ms^{-1}). This is because of the increased friction near the mountains. Besides, this corresponds to the thermal structure, because the strong elevated inversion layer inhibits the downward transfer of momentum. As a result, the horizontal transport capacity of the stations in the west is poorer than that of the stations in the east, which is another reason for the observed spatial distribution of haze pollution.

ABLH and AAL depth

The ABLH, as a reflection of the layer dominated by turbulent motion, is a crucial parameter in air quality assessment. The ABLH was determined at 14:00 LT and 5:00 LT, corresponding to the time when the ABL was fully developed in the daytime and stabilized at night, respectively. As the CBL is usually formed in the daytime and the SBL is formed at night, we use the CBL and SBL below. The temporal variations of the average heights of six stations of the CBL and SBL during the observation period are shown in Fig. 7. The average CBL height is below 560 m during the three haze episodes, compared with 910 m during clear periods. The average SBL height is ~ 280 m and 270 m during the haze episodes and clean periods, respectively. There is a significant

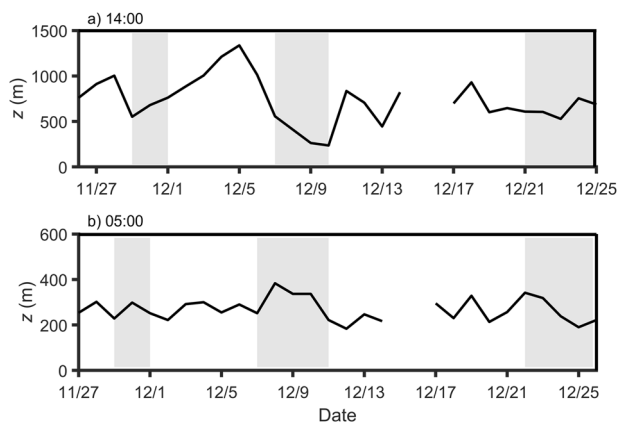


Fig. 7 Temporal variations of the average atmospheric boundary layer height of six observation stations during the observation period. **a** 14:00 LT and **b** 05:00 LT. The shaded areas represent three haze episodes.

decrease in the CBL height during haze pollution, which is associated with smaller sensible heat fluxes and may be attributed to cloudy weather and aerosol radiation effects, while the SBL height has little difference between haze and clean periods. As a consequence, it is mainly the suppression of CBL development that promotes the formation of haze pollution.

Figure 8a shows a comparison between the ABLH and AAL depth. It can be seen that the consistency between the AAL depth and the ABLH is higher during the day than that at night. The nighttime AAL depth is obviously higher than the ABLH. As shown in Fig. 8b, we further compared the AAL depth at 20:00 LT and the CBL height on the same day. After rejecting the data points in the relatively clean atmosphere during the early stage of pollution, or in the nonstationary atmosphere state in the rapid cleaning period of pollution (most of the points in the lower right in Fig. 8b, there is a relatively good correlation between the nighttime AAL depth and the CBL height on the same day. The correlation coefficient is 0.74, which is significant at the significant level of 5%.

Figure 9 gives an example that further illustrates the relationship between the AAL depth and the ABLH. This example indicates

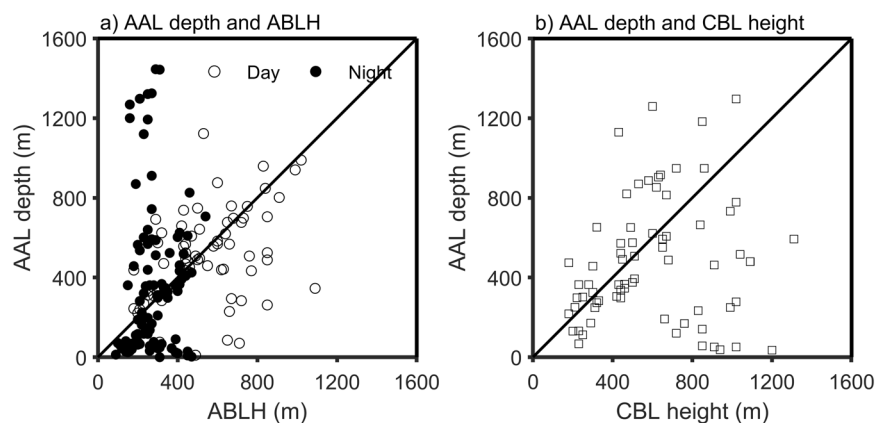


Fig. 8 Comparisons between the AAL depth and the ABLH. **a** the AAL depth and ABLH, **b** the nighttime AAL depth and the CBL height on the same day of six observation stations.

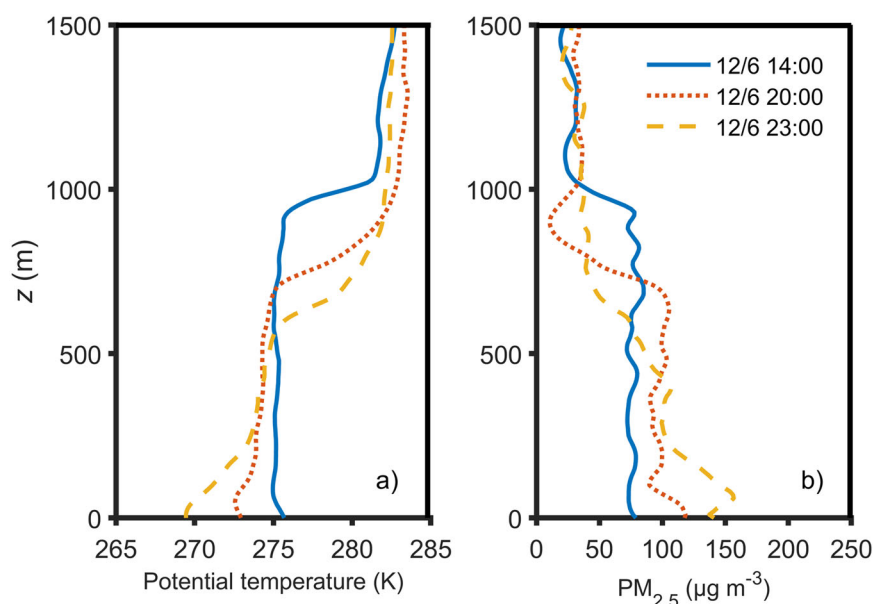


Fig. 9 Variations in the vertical distributions of potential temperature and air pollutants at Baoding station on 6 December 2019. **a** Potential temperature and **b** $PM_{2.5}$ concentration.

that in the unstable CBL (at 14:00 LT), aerosols can be well mixed by vertical turbulent transport throughout the boundary layer, and the AAL corresponds well with the CBL. While in the SBL at night (20:00 and 23:00 LT), the stable layer is approximately one or two hundred meters thick near the ground. Due to the weak turbulent mixing in the stable layer, aerosols accumulate near the surface and have an increase in surface concentration. However, since the aerosols remain suspended in upper layer (known as the residual layer), the variation of AAL depth corresponds with the residual layer top at night. In other words, unlike the thermal structure, which collapses after sunset and rebuilds by surface radiation cooling at night, aerosols can remain suspended in the air and maintain their daytime vertical distribution in the residual layer at night. As a consequence, the evolution of the AAL depth is not comparable to the diurnal variation of the ABLH because the AAL depth is consistent with the CBL height due to sufficient turbulent mixing during the day, but suggests the presence of the residual layer at night. This feature of the vertical aerosol distribution makes it difficult to accurately retrieve the SBL height using lidars or ceilometers based on the distributions of substances^{41,71,72}. In addition, considering only the effect of the ABL on the vertical diffusion of pollutants, the good consistency between the daytime ABLH and AAL depth occurs under the condition when the atmospheric motion is stationary and the turbulent mixing is sufficient that can make abundant pollutants from the ground distribute throughout the boundary layer. Therefore, using the daytime AAL depth retrieved by lidars to represent the CBL height also has preconditions.

DISCUSSION

From 26 November to 26 December 2019, an intensive field experiment was carried out simultaneously at six stations arranged in a cross shape in the North China Plain. Based on comprehensive observations, including both atmospheric profiles and surface meteorological elements, this study mainly focused on the following three questions. First, what are the impacts of the ABL structure on heavy haze pollution? Second, what are the characteristics of the spatial distribution of haze pollution and the regional ABL structure in this particular location of the NCP? Third, how does the AAL depth relate to the ABLH? The main results are as follows.

The meteorological elements and PM_{2.5} concentration profiles indicate that the vertical distribution of pollutants is greatly influenced by the ABL structure. A persistent descending elevated inversion layer is crucial to the maintenance and exacerbation of heavy haze pollution. This stable layer traps aerosols beneath it by inhibiting vertical turbulent transport, and the decreasing bottom height forces aerosols to accumulate in a shallower layer, resulting in worsened air quality. This descending elevated inversion layer may be attributed to bouts of downdrafts generated by the intrusion of gusty cold air. With regard to the dynamic structure of the ABL, weak winds (speeds smaller than 2 m s⁻¹) are dominant in the lower atmosphere during long-lasting haze pollution. The removal of pollutants is mainly due to the contribution of low-level jets which improve both the horizontal transport capacity and the vertical diffusion conditions. Furthermore, the aerosol accumulation layer corresponds to the water vapor-enriched layer, indicating the synchronous regional transport or local accumulation of both aerosols and water vapor.

The unique geographical location of the NCP is reflected in its particular regional ABL structure. Due to the nighttime drainage flow and warming effect induced by strong downdrafts, stations located in the west near the mountains have a colder surface and warmer upper air masses, resulting in a more stable stratification and worse diffusion conditions. Furthermore, due to the increased friction caused by the mountains, thicker layers with weaker winds also appear at the western stations. These differences in the ABL

structure further contribute to the uneven spatial distribution of haze pollution, with higher pollution levels in the western areas near the mountains and less pollution toward the east.

Finally, the CBL height significantly decreases during haze episodes, with an average height lower than 560 m. In contrast, the SBL height experiences little variation between haze and clean periods, mostly within 200–300 m. This suggests that it is mainly the suppression of CBL development that promotes haze pollution. Moreover, the AAL depth is relatively consistent with the CBL height but much higher than the SBL height. However, high consistency is shown between the nighttime AAL depth and the CBL height on the same day. This finding reveals that the vertical distribution of aerosols mainly depends on daytime thermal turbulent mixing and is maintained at night. As a consequence, it is more suitable to determine the ABLH from the distributions of substances in the daytime, but this method is not applicable at night due to the impact of the residual layer.

METHODS

Observation stations and instruments

The NCP, which is located in the northern part of eastern China, is surrounded by the Yanshan Mountains to the north, the Taihang Mountains to the west, and the Bohai Sea to the east (Fig. 1). As high-altitude terrain can block surface winds, a weak wind zone forms on the NCP^{6,13}. Besides, the semienclosed terrain on the eastern leeward slope is influenced by remarkable downdrafts in winter¹². Complex processes, such as mountain-plain breeze circulation, sea-land breeze circulation and the urban heat island effect^{14–17} can affect the ABL structure in the NCP, which further affect the spatiotemporal distribution of air pollutants^{18,19}. Some studies have found an inhomogeneous spatial distribution of pollution in the NCP^{27,70,73,74}. To investigate the unique ABL structure in the NCP and better understand the influence of the ABL structure on regional haze pollution, an intensive field experiment was conducted from 26 November to 26 December 2019 at six observation stations in Hebei Province, China. As shown in Fig. 1, the six observation stations were organized in a cross shape centered on the Baoding station. Perpendicular to the Taihang Mountains, four stations were deployed from west to east, namely, Tuonan (39°1′N, 115°7′E), Baoding (38°47′N, 115°30′E), Renqiu (38°44′N, 116°6′E), and Cangzhou (38°17′N, 116°50′E). Three stations were established along the Taihang Mountains, Dingzhou (38°34′N, 115°0′E) and Bazhou station (39°8′N, 116°26′E) located on the south and north sides of the Baoding station, respectively. All the stations were on the edge of the corresponding city. Except for Tuonan and Dingzhou stations, which were closer to the mountains with relatively high altitudes of ~190 m and 60 m, respectively, the altitudes of the other stations were lower than 20 m.

The instrumentation deployed at the observation sites is described as follows. Enhanced ground observations were arranged at the Tuonan, Baoding and Renqiu stations, and each site was equipped with a three-dimensional sonic anemometer-thermometer to obtain turbulence data and meteorological factors in the surface layer. Radiosonde observations and surface pressure observations were carried out at all six stations. Detailed information on each site is summarized in Table 1.

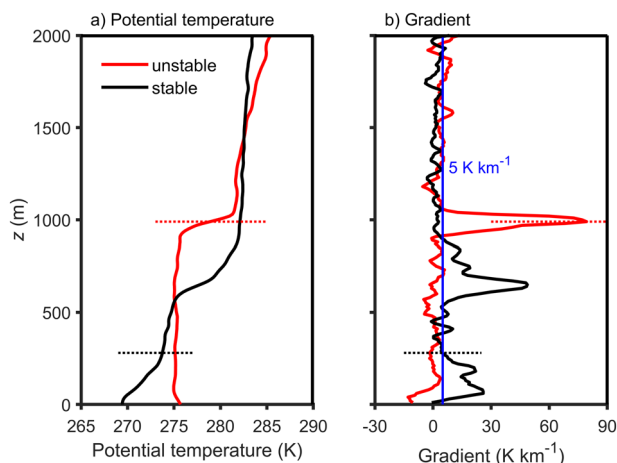
Data acquisition and processing

The turbulence data and surface meteorological factors were detected by three-dimensional sonic anemometer-thermometer devices, including IGRASON (Campbell Scientific, Inc., USA) for Baoding and Renqiu stations and CSAT3 (Campbell Scientific, Inc., USA) for Tuonan station. IGRASON integrates with a CO₂/H₂O gas analyzer which is absent from CSAT3, and therefore, there were no humidity observations at the Tuonan station. The original data were sampled at a frequency of 10 Hz and was averaged over an interval of 30 min.

The sounding data were obtained by a particulate sounding system, which comprises GPS radiosondes and portable particulate sensors. Detailed information on the sounding system has been described in Li Q. et al.⁷⁵. The sounding data contained both meteorological elements (temperature, relative humidity, wind speed and wind direction) and PM_{2.5} concentrations. Radiosonde observations were carried out every 3 h beginning at 14:00 LT on 26 November 2019 and ending at 11:00 LT on 26 December 2019. A total of 240 sets of profile data were collected at each station during the intensive observation period. We eliminated the

Table 1. The observation contents and corresponding periods at six stations.

Stations	Observation contents	Observation period
BD	Turbulence and meteorological elements	2019/12/3–2019/12/26;
	Sounding data and surface pressure	2019/11/26–2019/12/26
TN	Turbulence and meteorological elements	2019/12/6–2019/12/26;
	Sounding data and surface pressure	2019/11/26–2019/12/26
RQ	Turbulence and meteorological elements	2019/11/26–2019/12/26;
	Sounding data and surface pressure	2019/11/26–2019/12/26
CZ	Sounding data and surface pressure	2019/11/26–2019/12/26
BZ	Sounding data and surface pressure	2019/11/26–2019/12/26
DZ	Sounding data and surface pressure	2019/11/26–2019/12/26

**Fig. 10** Schematic diagram of ABLH determination under different stratification conditions. **a** Typical thermal structure of the ABL under unstable and stable conditions; **b** The potential temperature gradient corresponding to the profiles in **a**.

outliers from the original data and applied a moving average to the data. Considering the low ABLH in winter, we extracted the data from 0 to 2000 m and processed the data into a vertical resolution of 10 m.

The surface pressure data were collected by barometric pressure sensors (CS106, Campbell Scientific, Inc., USA). The observations were automatic and continuous with a temporal resolution of 10 min, and the original data were processed into averages with an interval of 30 min. The pressure at different heights was calculated based on the barometric height formula. Combined with the temperature and relative humidity observed by GPS sounding, the potential temperature and specific humidity were further calculated.

In addition to the data from our observations, we used the AQI data from the China National Environmental Monitoring Station. The hourly averaged AQI data were released in real-time and it can be downloaded from <http://www.cnemc.cn/sss/>. Furthermore, the vertical velocity reanalysis data we used were downloaded from ERA5 (<https://www.ecmwf.int/en/forecasts/datasets/reanalysis-datasets/era5>). The temporal resolution is 1 h and the horizontal resolution is $0.25^\circ \times 0.25^\circ$.

Determination of the ABLH and AAL depth

Because of differences in the thermodynamic properties and turbulent characteristics, the ABL structure is quite different between the daytime and nighttime. During the daytime, the CBL has an unstable stratification with active turbulence due to surface heating. While during the nighttime, the SBL characterized by a surface-based inversion layer is formed by surface radiative cooling, and intermittent turbulence often happens in it. The ABLH can be determined by the thermodynamic approach, that is, recognizing the boundary layer top according to the variation in the gradient of the potential temperature^{76,77}. In the daytime, the potential

temperature mixed nearly uniform in the ABL and has a large temperature gradient in the entrainment layer. We take the position of the entrainment layer as the CBL top. In the nighttime, the depth of the surface-based inversion layer is recognized as the height of SBL. Figure 10 is a schematic diagram of ABLH determination. We first calculate the potential temperature difference between 100 m and the surface to judge whether the boundary layer type is stable or unstable. If it is unstable, then we identify the location of entrainment layer by finding the peak height of potential temperature gradient greater than $10 K km^{-1}$. If it is stable stratification, due to the potential temperature gradient decreasing upward from the ground, we identify the height where the potential temperature gradient is close to zero as the boundary layer top. As the average potential temperature gradient above 500 m is $\sim 5 K km^{-1}$, we use $5 K km^{-1}$ as the threshold to find SBL top in practice. During the observation period, there was precipitation on 15 to 16 December, and thus, these two days were not considered.

The height determined from the distribution of substances essentially reflects the maximum vertical diffusion depth of aerosols, which is distinct from the height determined by meteorological elements^{78,79}. To distinguish this height from the traditional boundary layer, which is derived from turbulent motion, we propose the aerosol accumulation layer to emphasize the properties of the vertical distribution of aerosols. According to the National Environmental Protection Standards of China, the air is polluted when $PM_{2.5}$ concentration is higher than $75 \mu g m^{-3}$. Therefore, we define the AAL as the layer abundant in aerosols with $PM_{2.5}$ concentrations higher than $75 \mu g m^{-3}$ above the surface.

DATA AVAILABILITY

The AQI data used in this study are downloaded from <http://www.cnemc.cn/sss/>. The reanalysis data used in this study are available from ERA5 (<https://www.ecmwf.int/en/forecasts/datasets/reanalysis-datasets/era5>). The observational data used in this study are available from the corresponding author upon reasonable request (hsdq@pku.edu.cn).

CODE AVAILABILITY

All computer codes used to generate results in the paper are available from the corresponding author upon reasonable request.

Received: 18 August 2020; Accepted: 23 January 2021;

Published online: 22 February 2021

REFERENCES

1. Quan, J. et al. Analysis of the formation of fog and haze in North China Plain (NCP). *Atmos. Chem. Phys.* **11**, 8205–8214 (2011).
2. Zhang, Y. L. & Cao, F. Fine particulate matter (PM_{2.5}) in China at a city level. *Sci. Rep.* **5**, 14884 (2015).
3. Cheng, Z. et al. Status and characteristics of ambient PM_{2.5} pollution in global megacities. *Environ. Int.* **89–90**, 212–221 (2016).
4. Chai, F. et al. Spatial and temporal variation of particulate matter and gaseous pollutants in 26 cities in China. *J. Environ. Sci.* **26**, 75–82 (2014).

5. Wang, Y., Ying, Q., Hu, J. & Zhang, H. Spatial and temporal variations of six criteria air pollutants in 31 provincial capital cities in China during 2013–2014. *Environ. Int.* **73**, 413–422 (2014).
6. Wang, X., Dickinson, R. E., Sun, L., Zhou, C. & Wang, K. PM_{2.5} pollution in China and how it has been exacerbated by terrain and meteorological conditions. *Bull. Am. Meteorol. Soc.* **99**, 105–119 (2018).
7. Li, X. et al. Particulate matter pollution in Chinese cities: Areal-temporal variations and their relationships with meteorological conditions (2015–2017). *Environ. Pollut.* **246**, 11–18 (2019).
8. Chan, C. K. & Yao, X. Air pollution in mega cities in China. *Atmos. Environ.* **42**, 1–42 (2008).
9. Zhang, X. Y. et al. Atmospheric aerosol compositions in China: spatial/temporal variability, chemical signature, regional haze distribution and comparisons with global aerosols. *Atmos. Chem. Phys.* **12**, 779–799 (2012).
10. Ni, Z. Z. et al. Assessment of winter air pollution episodes using long-range transport modeling in Hangzhou, China, during World Internet Conference, 2015. *Environ. Pollut.* **236**, 550–561 (2018).
11. Zhao, S. et al. Two winter PM_{2.5} pollution types and the causes in the city clusters of Sichuan Basin, Western China. *Sci. Total Environ.* **636**, 1228–1240 (2018).
12. Zhu, W. et al. The characteristics of abnormal wintertime pollution events in the Jing-Jin-Ji region and its relationships with meteorological factors. *Sci. Total Environ.* **626**, 887–898 (2018).
13. Xu, X. D. et al. “Harbor” effect of large topography on haze distribution in eastern China and its climate modulation on decadal variations in haze. *Chin. Sci. Bull.* **60**, 1132–1143 (2015).
14. Miao, S. et al. An observational and modeling study of characteristics of urban heat island and boundary layer structures in Beijing. *J. Appl. Meteorol. Climatol.* **48**, 484–501 (2009).
15. Miao, Y. et al. Numerical study of the effects of local atmospheric circulations on a pollution event over Beijing–Tianjin–Hebei, China. *J. Environ. Sci.* **30**, 9–20 (2015).
16. Chen, Y. et al. Aircraft study of mountain chimney effect of Beijing, China. *J. Geophys. Res.* **114**, D08306 (2009).
17. Hu, X. M. et al. Impact of the Loess Plateau on the atmospheric boundary layer structure and air quality in the North China Plain: A case study. *Sci. Total Environ.* **499**, 228–237 (2014).
18. Jazcilevich, A. D. et al. Locally induced surface air confluence by complex terrain and its effects on air pollution in the valley of Mexico. *Atmos. Environ.* **39**, 5481–5489 (2005).
19. Ning, G. et al. Characteristics of air pollution in different zones of Sichuan Basin, China. *Sci. Total Environ.* **612**, 975–984 (2018).
20. Tai, A. P. K., Mickley, L. J. & Jacob, D. J. Correlations between fine particulate matter (PM_{2.5}) and meteorological variables in the United States: Implications for the sensitivity of PM_{2.5} to climate change. *Atmos. Environ.* **44**, 3976–3984 (2010).
21. Ji, D. et al. The heaviest particulate air-pollution episodes occurred in northern China in January, 2013: Insights gained from observation. *Atmos. Environ.* **92**, 546–556 (2014).
22. Wang, H. J. & Chen, H. P. Understanding the recent trend of haze pollution in eastern China: roles of climate change. *Atmos. Chem. Phys.* **16**, 4205–4211 (2016).
23. Li, M. et al. Exploring the regional pollution characteristics and meteorological formation mechanism of PM_{2.5} in North China during 2013–2017. *Environ. Int.* **134**, 105283 (2020).
24. Ren, Y., Zhang, H., Wei, W., Cai, X. & Song, Y. Determining the fluctuation of PM_{2.5} mass concentration and its applicability to Monin–Obukhov similarity. *Sci. Total Environ.* **710**, 136398 (2020).
25. Zhao, B. et al. A high-resolution emission inventory of primary pollutants for the Huabei region, China. *Atmos. Chem. Phys.* **12**, 481–501 (2012).
26. Gao, J. et al. Temporal-spatial characteristics and source apportionment of PM_{2.5} as well as its associated chemical species in the Beijing–Tianjin–Hebei region of China. *Environ. Pollut.* **233**, 714–724 (2018).
27. Cai, S. et al. The impact of the “Air Pollution Prevention and Control Action Plan” on PM_{2.5} concentrations in Jing-Jin-Ji region during 2012–2020. *Sci. Total Environ.* **580**, 197–209 (2017).
28. Chen, H. & Wang, H. Haze Days in North China and the associated atmospheric circulations based on daily visibility data from 1960 to 2012. *J. Geophys. Res.* **120**, 5895–5909 (2015).
29. Ye, X., Song, Y., Cai, X. & Zhang, H. Study on the synoptic flow patterns and boundary layer process of the severe haze events over the North China Plain in January 2013. *Atmos. Environ.* **124**, 129–145 (2016).
30. Liao, T. et al. Air stagnation and its impact on air quality during winter in Sichuan and Chongqing, southwestern China. *Sci. Total Environ.* **635**, 576–585 (2018).
31. Jiang, C., Wang, H., Zhao, T., Li, T. & Che, H. Modeling study of PM_{2.5} pollutant transport across cities in China’s Jing–Jin–Ji region during a severe haze episode in December 2013. *Atmos. Chem. Phys.* **15**, 5803–5814 (2015).
32. Sun, Y. et al. Rapid formation and evolution of an extreme haze episode in Northern China during winter 2015. *Sci. Rep.* **6**, 27157 (2016).
33. Jin, X. et al. Diagnostic analysis of wintertime PM_{2.5} pollution in the North China Plain: The impacts of regional transport and atmospheric boundary layer variation. *Atmos. Environ.* **224**, 117346 (2020).
34. Guo, S. et al. Elucidating severe urban haze formation in China. *Proc. Natl Acad. Sci. USA* **111**, 17373–17378 (2014).
35. Huang, R. J. et al. High secondary aerosol contribution to particulate pollution during haze events in China. *Nature* **514**, 218–222 (2014).
36. Li, J. et al. Insight into the formation and evolution of secondary organic aerosol in the megacity of Beijing, China. *Atmos. Environ.* **220**, 117070 (2020).
37. Miao, Y. et al. Interaction between planetary boundary layer and PM_{2.5} pollution in megacities in China: a review. *Curr. Pollut. Rep.* **5**, 261–271 (2019).
38. Wang, L. et al. Impacts of the near-surface urban boundary layer structure on PM_{2.5} concentrations in Beijing during winter. *Sci. Total Environ.* **669**, 493–504 (2019).
39. Wei, W. et al. Influence of intermittent turbulence on air pollution and its dispersion in winter 2016/2017 over Beijing, China. *J. Meteorol. Res.* **34**, 176–188 (2020).
40. Li, X. B., Wang, D. S., Lu, Q. C., Peng, Z. R. & Wang, Z. Y. Investigating vertical distribution patterns of lower tropospheric PM_{2.5} using unmanned aerial vehicle measurements. *Atmos. Environ.* **173**, 62–71 (2018).
41. Liu, C. et al. Vertical distribution of PM_{2.5} and interactions with the atmospheric boundary layer during the development stage of a heavy haze pollution event. *Sci. Total Environ.* **704**, 135329 (2020).
42. Sun, T. et al. Aerosol optical characteristics and their vertical distributions under enhanced haze pollution events: effect of the regional transport of different aerosol types over eastern China. *Atmos. Chem. Phys.* **18**, 2949–2971 (2018).
43. Luan, T., Guo, X., Guo, J. & Zhang, T. Quantifying the relationship between PM_{2.5} concentration, visibility and planetary boundary layer height for long-lasting haze and fog–haze mixed events in Beijing. *Atmos. Chem. Phys.* **18**, 203–225 (2018).
44. Ren, Y. et al. Effects of turbulence structure and urbanization on the heavy haze pollution process. *Atmos. Chem. Phys.* **19**, 1041–1057 (2019).
45. Xu, T. et al. Temperature inversions in severe polluted days derived from radio-sonde data in North China from 2011 to 2016. *Sci. Total Environ.* **647**, 1011–1020 (2019).
46. Sun, Y., Song, T., Tang, G. & Wang, Y. The vertical distribution of PM_{2.5} and boundary-layer structure during summer haze in Beijing. *Atmos. Environ.* **74**, 413–421 (2013).
47. Quan, J. et al. Regional atmospheric pollutant transport mechanisms over the North China Plain driven by topography and planetary boundary layer processes. *Atmos. Environ.* **221**, 117098 (2020).
48. Li, X. et al. Impact of planetary boundary layer structure on the formation and evolution of air-pollution episodes in Shenyang, Northeast China. *Atmos. Environ.* **214**, 116850 (2019).
49. Wei, W. et al. Intermittent turbulence contributes to vertical dispersion of PM_{2.5} in the North China Plain: cases from Tianjin. *Atmos. Chem. Phys.* **18**, 12953–12967 (2018).
50. Ren, Y. et al. A study on atmospheric turbulence structure and intermittency during heavy haze pollution in the Beijing area. *Sci. China Earth Sci.* **62**, 2058–2068 (2019).
51. Zhang, H. et al. Research progress on estimation of the atmospheric boundary layer height. *J. Meteorol. Res.* **34**, 482–498 (2020).
52. Gui, K. et al. Satellite-derived PM_{2.5} concentration trends over Eastern China from 1998 to 2016: relationships to emissions and meteorological parameters. *Environ. Pollut.* **247**, 1125–1133 (2019).
53. Quan, J. et al. Evolution of planetary boundary layer under different weather conditions, and its impact on aerosol concentrations. *Particuology* **11**, 34–40 (2013).
54. Liu, N., Zhou, S., Liu, C. & Guo, J. Synoptic circulation pattern and boundary layer structure associated with PM_{2.5} during wintertime haze pollution episodes in Shanghai. *Atmos. Res.* **228**, 186–195 (2019).
55. Miao, Y., Liu, S. & Huang, S. Synoptic pattern and planetary boundary layer structure associated with aerosol pollution during winter in Beijing, China. *Sci. Total Environ.* **682**, 464–474 (2019).
56. Tang, G. et al. Mixing layer height and its implications for air pollution over Beijing, China. *Atmos. Chem. Phys.* **16**, 2459–2475 (2016).
57. Zhao, H. et al. Climatology of mixing layer height in China based on multi-year meteorological data from 2000 to 2013. *Atmos. Environ.* **213**, 90–103 (2019).
58. Eresmaa, N., Karppinen, A., Joffre, S. M., Räsänen, J. & Talvitie, H. Mixing height determination by ceilometer. *Atmos. Chem. Phys.* **6**, 1485–1493 (2006).
59. Yang, T. et al. Boundary layer height determination from lidar for improving air pollution episode modeling: development of new algorithm and evaluation. *Atmos. Chem. Phys.* **17**, 6215–6225 (2017).

60. Su, T., Li, Z. & Kahn, R. A new method to retrieve the diurnal variability of planetary boundary layer height from lidar under different thermodynamic stability conditions. *Remote Sens. Environ.* **237**, 111519 (2020).
61. Emeis, S. & Schäfer, K. Remote sensing methods to investigate boundary-layer structures relevant to air pollution in cities. *Bound. Layer. Meteorol.* **121**, 377–385 (2006).
62. Han, S. et al. Boundary layer structure and scavenging effect during a typical winter haze-fog episode in a core city of BTH region, China. *Atmos. Environ.* **179**, 187–200 (2018).
63. Miao, Y. et al. Unraveling the relationships between boundary layer height and PM2.5 pollution in China based on four-year radiosonde measurements. *Environ. Pollut.* **243**, 1186–1195 (2018).
64. Wang, L. et al. Vertical observations of the atmospheric boundary layer structure over Beijing urban area during air pollution episodes. *Atmos. Chem. Phys.* **19**, 6949–6967 (2019).
65. Xu, Y., Zhu, B., Shi, S. & Huang, Y. Two inversion layers and their impacts on PM2.5 concentration over the Yangtze River Delta, China. *J. Appl. Meteorol. Climatol.* **58**, 2349–2362 (2019).
66. Chen, Z. et al. Relationship between atmospheric pollution processes and synoptic pressure patterns in northern China. *Atmos. Environ.* **42**, 6078–6087 (2008).
67. Silcox, G. D., Kelly, K. E., Crosman, E. T., Whiteman, C. D. & Allen, B. L. Wintertime PM2.5 concentrations during persistent, multi-day cold-air pools in a mountain valley. *Atmos. Environ.* **46**, 17–24 (2012).
68. Han, X., Zhang, M., Zhu, L. & Skorokhod, A. Assessment of the impact of emissions reductions on air quality over North China Plain. *Atmos. Pollut. Res.* **7**, 249–259 (2016).
69. Guo, L., Guo, X., Fang, C. & Zhu, S. Observation analysis on characteristics of formation, evolution and transition of a long-lasting severe fog and haze episode in North China. *Sci. China Earth Sci.* **58**, 329–344 (2015).
70. Zhang, C., Wang, Y., Zhang, H. & Zhao, B. Temporal and spatial distribution of PM2.5 and PM10 pollution status and the correlation of particulate matters and meteorological factors during winter and spring in Beijing. *Environ. Sci.* **35**, 418–427 (2014). in Chinese.
71. Wang, Z. et al. Lidar measurement of planetary boundary layer height and comparison with microwave profiling radiometer observation. *Atmos. Meas. Tech.* **5**, 1965–1972 (2012).
72. Lee, J. et al. Ceilometer monitoring of boundary-layer height and its application in evaluating the dilution effect on air pollution. *Bound. Layer. Meteorol.* **172**, 435–455 (2019).
73. Yu, M., Cai, X., Xu, C. & Song, Y. A climatological study of air pollution potential in China. *Theor. Appl. Climatol.* **136**, 627–638 (2019).
74. Li, R. et al. Diurnal, seasonal and spatial variation of PM2.5 in Beijing. *Sci. Bull.* **60**, 387–395 (2015).
75. Li, Q. et al. Characteristics of the atmospheric boundary layer and its relation with PM2.5 during haze episodes in winter in the North China Plain. *Atmos. Environ.* **223**, 117265 (2020).
76. Dai, C. et al. Determining boundary-layer height from aircraft measurements. *Bound. Layer. Meteorol.* **152**, 277–302 (2014).
77. Zhang, H. et al. Research progress on estimation of atmospheric boundary layer height. *Acta Meteorol. Sin.* **78**, 522–536 (2020). in Chinese.
78. Caicedo, V. et al. Comparison of aerosol lidar retrieval methods for boundary layer height detection using ceilometer aerosol backscatter data. *Atmos. Meas. Tech.* **10**, 1609–1622 (2017).
79. Shi, Y., Hu, F., Xiao, Z., Fan, G. & Zhang, Z. Comparison of four different types of planetary boundary layer heights during a haze episode in Beijing. *Sci. Total Environ.* **711**, 134928 (2020).

ACKNOWLEDGEMENTS

This work was jointly funded by grant from National Key R&D Program of China (2017YFC0209600, 2016YFC0203300), and the National Natural Science Foundation of China (91837209, 41705003, 91544216).

AUTHOR CONTRIBUTIONS

Q.L. analyzed experimental data, wrote, and edited the manuscript. H.Z. designed experiments, wrote, and edited the manuscript. X.C. designed experiments and participated in discussions of the result. Y.S. and T.Z. contributed to discussions of the results and the manuscript.

COMPETING INTERESTS

The authors declare no competing interests.

ADDITIONAL INFORMATION

Correspondence and requests for materials should be addressed to H.Z.

Reprints and permission information is available at <http://www.nature.com/reprints>

Publisher's note Springer Nature remains neutral with regard to jurisdictional claims in published maps and institutional affiliations.



Open Access This article is licensed under a Creative Commons Attribution 4.0 International License, which permits use, sharing, adaptation, distribution and reproduction in any medium or format, as long as you give appropriate credit to the original author(s) and the source, provide a link to the Creative Commons license, and indicate if changes were made. The images or other third party material in this article are included in the article's Creative Commons license, unless indicated otherwise in a credit line to the material. If material is not included in the article's Creative Commons license and your intended use is not permitted by statutory regulation or exceeds the permitted use, you will need to obtain permission directly from the copyright holder. To view a copy of this license, visit <http://creativecommons.org/licenses/by/4.0/>.

© The Author(s) 2021